A Time- and Temperature-Dependent 2-D Simulation of the GTO Thyristor Turn-Off Process

AKIO NAKAGAWA, MEMBER, IEEE, AND DAVID H. NAVON, SENIOR MEMBER, IEEE

Abstract—GTO thyristor turn-off process is analyzed for a resistive load case by performing an exact two-dimensional time- and temperature-dependent numerical simulation. A newly defined concept "on-region" is introduced to help understanding of the simulation results.

Excess carrier plasma (on-region) in the p-base is squeezed finally to as narrow as 60 μm wide, accompanying a large current density increase at the center of the middle junction. The carriers in the n-base are found not to be greatly affected by the initial plasma squeezing in the p-base. After the on-region width in the p-base reaches its final limit, the excess carriers around the middle junction of the final on-region is rapidly reduced, resulting in complete anode current turn-off.

I. Introduction

RECENT advances in GTO thyristor development have enabled the devices to be operated at more than 1000 A and 2500 V [1], [2]. These devices can be realized by an appropriate combination of reduced p-base sheet resistance [3], thicker n-base layer [4], increased gate-cathode breakdown voltage [5], anode short circuit [6], etc. All these parameters affect the maximum interruptable anode current, which determines the current rating of the device directly because improper turn-off behavior may cause fatal damage to the device.

In contrast to reports of advances in the device fabrication, there have been only a small number of publications on the failure mechanism analysis [4]. It was also very recent that the numerical technique was applied to a thyristor [7], [8], [9]. There were only several papers published regarding a GTO thyristor. In 1979, Naito *et al.* [10] analyzed a GTO turn-off process making use of a 1-D model. In 1981, Nakagawa [11] analyzed the abnormal characteristic that a GTO with a heavily doped p-base exhibits as sudden forward voltage increases over a critical current density. The same author [12] also analyzed the current concentration during the turn-off process, using a 1-D model, which included the effects of the conduction region squeezing as well as the temperature increase. In 1981, a 2-D model was presented by Shimizu *et al.* [13] for analyzing the steady-state characteristics. Such a 2-D model is inevitable for the accurate GTO turn-off simulation because it is accompanied by the squeezing of the "on-region" (see Section III for the definition). Moreover, the model should deal with 4 basic device equations [14], [15], including the heat equation, which is necessary for the GTO turn-off failure analysis. In the present paper, such a 2-D model with 4 equations is applied to a GTO turn-off process to obtain new insight into the squeezing of the "on-region."

Manuscript received May 3, 1983; revised March 30, 1984.

A. Nakagawa is with the Toshiba Research and Development Center, Kawasaki 210, Japan.

D. H. Navon is with the Electrical and Computer Engineering Department, University of Massachusetts, Amherst, MA 01003.

II. Mathematical Model

In order to simulate exact device characteristics, various higher order effects such as heavy doping effects (H.D.E.), Fermi statistics, carrier-carrier scattering, Auger recombination etc., have to be included. As for heavy doping effects, bandgap narrowing modeling was first introduced by De Man [16] in 1971. Since then, there have been numerous publications on this effect [16], [17], [18], [19], [20], [21]. There are two different methods proposed to formulate the current equations under position-dependent bandgap variation. One is expressed in terms of the two band edge changes, ΔV_c, ΔV_v [17], and the other is in terms of the intrinsic concentration, n_i [18].

$$J_n = \mu_n kT \frac{\partial n}{\partial x} - q\mu_n n \frac{\partial}{\partial x}(\psi + \Delta V_c). \tag{1}$$

$$J_n = \mu_n kT \frac{\partial n}{\partial x} - q\mu_n n \frac{\partial}{\partial x}\left(\psi + \frac{kT}{q} \ln n_i + \omega\right). \tag{2}$$

These two equations are equivalent only under the Boltzmann statistics approximation and isothermal conditions. However, for a heavily doped silicon, Boltzmann statistics are not valid; neither is the following equation which offers the basis for the equivalence of the two equations.

$$n_i^2 = N_{v0} \cdot N_{c0} \exp - \frac{q}{kT}(V_G - \Delta V_c - \Delta V_v). \tag{3}$$

N_{v0} and N_{c0} denote effective density of states for nondoped silicon. The following method, proposed in [21], enables an efficient simultaneous inclusion of both H.D.E. and Fermi statistics. The two characteristic parameters, ω_n and ω_p or n_i and ω, are defined by (4)–(7).

$$n = N_{c0} \exp \frac{q}{kT}(V_{c0} - \phi_n + \omega_n)$$

$$\equiv \int \frac{\rho(E)\, dE}{1 + \exp \frac{1}{kT}(E + q\phi_n)} \tag{4}$$

0018-9383/84/0900-1156$01.00 © 1984 IEEE

$$p = N_{v0} \exp \frac{q}{kT} (\phi_p - V_{v0} + \omega_p)$$

$$\equiv \int \frac{\rho(E')\, dE'}{1 + \exp \frac{1}{kT} (E' - q\phi_p)} \tag{5}$$

$$n_i = \sqrt{N_{c0} \cdot N_{v0}} \exp \frac{q}{2kT} (\omega_n + \omega_p + V_{c0} - V_{c0}) \tag{6}$$

$$\omega = (\omega_n - \omega_p)/2 + \frac{1}{2q} \left(\ln \frac{N_{c0}}{N_{v0}} \right) \tag{7}$$

where $-qV_{c0}$ and $-qV_{v0}$ represent the conduction band and valance band edge energies for nondoped silicon, respectively. These definitions, together with (8), lead to the Boltzmann-like equations (9) to (11) for the case of isothermal conditions in spite of the degeneracy.

$$\Psi = \psi + \omega, \quad (\psi = \tfrac{1}{2}(V_{c0} + V_{v0})) \tag{8}$$

$$J_n = \mu_n kT \frac{\partial n}{\partial x} - q\mu_n n \frac{\partial}{\partial x} \left(\Psi + \frac{kT}{q} \ln n_i \right) \tag{9}$$

$$J_p = -\mu_p kT \frac{\partial p}{\partial x} - q\mu_p p \frac{\partial}{\partial x} \left(\Psi - \frac{kT}{q} \ln n_i \right) \tag{10}$$

$$\frac{\epsilon}{q} \frac{\partial^2 \Psi}{\partial x^2} = n - p + \left(N_A - N_D + \frac{\epsilon}{q} \frac{\partial^2 \omega}{\partial x^2} \right) \tag{11}$$

$$n = n_i \exp \frac{q}{kT} (\Psi - \phi_n) \tag{12}$$

$$p = n_i \exp \frac{q}{kT} (\phi_p - \Psi). \tag{13}$$

ω is usually a small value, compared with the electrostatic potential, as is seen in actual calculations in [18], [21]. The last term $\epsilon/q(\partial^2\omega/\partial x^2)$ in (11) can be ignored compared with the term $N_A - N_D$. Also, Ψ can be treated as if it were a pure electrostatic potential [21]. These approximations hardly affect the terminal current-voltage relationship [22] since the usual boundary condition specifies n, p, ϕ_n, and ϕ_p values, and Ψ is precisely determined through (12), (13).

Another new parameter w is introduced for later use.

$$w = \tfrac{1}{2}(\omega_n + \omega_p). \tag{14}$$

Then, the basic equations for silicon are

$$J_n = \mu_n kT \frac{\partial n}{\partial x} - q\mu_n n \frac{\partial}{\partial x} (\Psi + w) \tag{15}$$

$$J_p = -\mu_p kT \frac{\partial p}{\partial x} - q\mu_p p \frac{\partial}{\partial x} (\Psi - w) \tag{16}$$

and

$$\frac{\partial^2 \Psi}{\partial x^2} = n - p + (N_A - N_D). \tag{17}$$

These equations are extended to the non-isothermal case. If the rigid band approximation is adopted for simplicity, a similar derivation to that in [23] gives rise to two additional current terms to (15). The first term is so called thermal diffusion [23] and is described by (18).

$$J_{th} = \left(\mu_{2n} - \frac{3}{2} \mu_n \right) kn \frac{\partial T}{\partial x}. \tag{18}$$

The definition of μ_{2n} can be found in the reference and is equal to $2\mu_n$ if acoustic scattering is the major scattering phenomena. It is necessary to be careful that this equation should be added to (15) not to (9) because (9) already includes the latter term of (18) ($-\frac{3}{2}\mu_n kn(\partial T/\partial x)$) in itself. The other current term is due to the variation in the bandgap energy with temperature [12] and should be included within parameter w. By denoting the value of w at room temperature by w_0, the w for temperature T will be given by

$$w = w_0 + s(T - T_0), \quad 2s = 2.82 \times 10^{-4} \text{ (V/degree) [24]}. \tag{19}$$

It can be shown that parameter s is the same for any impurity concentration of less than 1×10^{19} (cm^{-3}) [12].

Thus the final current equations may be expressed in the following way.

$$J_n = \mu_n kT \frac{\partial n}{\partial x} - q\mu_n n \frac{\partial}{\partial x} \Psi_e \tag{20}$$

$$J_p = -\mu_p kT \frac{\partial p}{\partial x} - q\mu_p p \frac{\partial}{\partial x} \Psi_h \tag{21}$$

$$\Psi_e = \Psi + w_0 + \left(s - \frac{k}{2q} \right) T \tag{22}$$

$$\Psi_h = \Psi - w_0 - \left(s - \frac{k}{2q} \right) T. \tag{23}$$

The temperature dependence of the carrier mobilities is given by the same formula as that developed in [12], which were determined from experimental data [25].

Solution Method

If Ψ does not change rapidly, the effective electric field $\partial\Psi_e/\partial x$ and $\partial\Psi_h/\partial x$ can be regarded as constant between two grid points and the conventional discretization method can be used by replacing Ψ by Ψ_e or Ψ_h. An independent variable set (n, p, Ψ, T) is used because of its programming feasibility. There was almost no difference observed in the convergence rate even if another set was chosen.

Newton's method was used to solve the nonlinear part of (20)-(23); SLOR (Successive Line Overrelaxation Method [26]) and the direct method were tried to solve the large number of linearized equations. In the actual program, (n, p, Ψ) are solved simultaneously, and the temperature equation is separately solved by Stone's method. However, it should be emphasized that the final complete simultaneous solutions were reached at each time step by iterating the two solution processes (Gummel's method). This is one distinction from the previous models [14], [15].

It was found that if the number of grid points for either of the two directions is small enough, then the direct method reaches convergence in less computer time than SLOR. Comparing the number of multiplications between the two programs, a criteria for the superiority of direct method over SLOR was found

$$N_{\min} < \sqrt{1.4f} \tag{24}$$

where N_{min} represents the smaller number of the grid lines in either of the two directions and f represents the number of SLOR iterations. In the present paper, a 7×55 ($X \times Y$) grid structure was adopted for the GTO turn-off process calculation. Thus the criteria becomes $f > 35$. Usually, as 1 Newton cycle requires 30 or 35 SLOR iterations, then the direct method gives convergence in almost the same time as SLOR. Moreover, the direct method is free of the relaxation parameter. The method referred to as the direct method actually means Gaussian elimination, which is used to obtain the U-matrix out of the original Jacobian matrix. This method can reduce the memory size to half that required by the LU-decomposition method. The numbering of grid points was done in such a way that adjacent grid points in the x-direction have consecutive numbers. This numbering method makes for an easier Gaussian elimination than the other.

The derivatives of mobilities as a function of electric potential should be included to attain rapid convergence. However, this is not an easy task because electric field magnitude at point M in Fig. 1 should be calculated by using the 6 ψ values for the points A, B, C, G, E, and I. It follows that the current equation associated with point B must involve the 9 adjacent points, resulting in a large amount of memory size and computer time. In the present paper, this situation was improved by using only 7 grid points without F and I. The electric magnitude for point M is calculated by (25).

$$E_M^2 = \left(\frac{\psi_E - \psi_B}{X_M}\right)^2 + \left(\frac{\psi_G - \psi_E}{Y_J}\right)^2. \tag{25}$$

As the mobility slowly changes with electric field E_M, the error associated with this is relatively small.

Initial Values

It was found very important to obtain initial values as close to the next solution as possible. In the model, the latest 3 solutions (last 3 time steps) were used to determine the trial values for the next solutions. These efforts can reduce the number of the Newton iterations. One way of doing this is to use 2nd order polynomials fitted to the last 3 solutions, where the variables are expressed in terms of Ψ, ln n, ln p, and T.

Boundary Conditions

Fig. 2 shows the whole device structure and the modeled region, which is actually a part of the real GTO device. There is no difference in the doping concentration in the x-direction and only 7 grid points are assigned to that direction. A special boundary condition is assumed for the gate contact so that the change in the carrier densities in the gate contact is allowed to closely simulate the actual device. The adopted boundary condition is of a current control type, where only gate current value is specified and the electric potential is automatically determined according to the operating condition. Thus it is possible that even the surface where the gate contact is formed has the same doping profile as that of the interior and represents one section of the device. The actual formulation will be interpreted, making use of Fig. 3. For example, current continuity equation for the point (4, 1) is given by the following

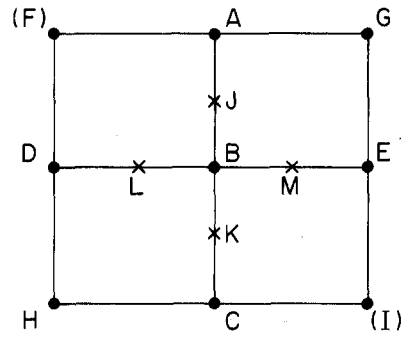

Fig. 1. Grid structure for 7 point discretization method.

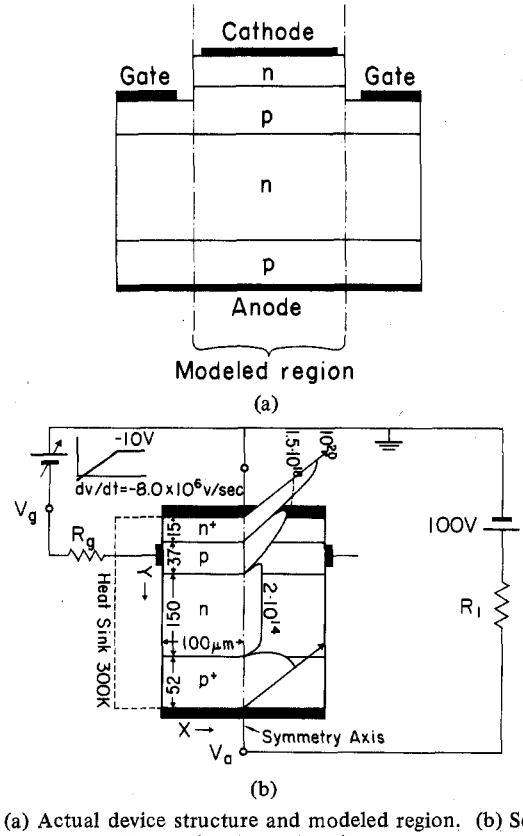

Fig. 2. (a) Actual device structure and modeled region. (b) Schematic diagram for the analyzed system.

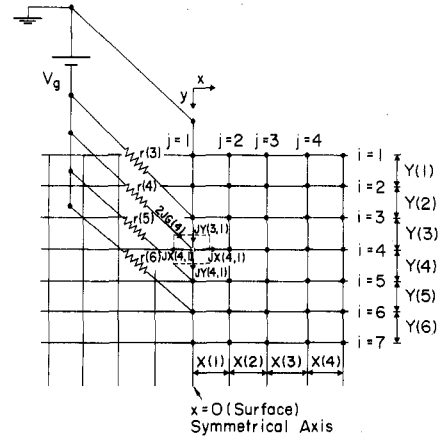

Fig. 3. Boundary conditions for the gate contact. (Dotted line shows the contour for Gauss's integral).

equation if Gauss's integral is applied to the boundary denoted by the dotted lines.

$$[JY(4,1) - JY(3,1)] \cdot 0.5 \cdot X(1) + JX(4,1) \cdot 0.5 \cdot [Y(3) + Y(4)] - JG(4) = -q \cdot R(4,1) \cdot 0.25 \cdot X(1) \cdot [Y(3) + Y(4)] \tag{26}$$

$$JG(4) = (-\phi_p(4,1) + V_g)/r(4) \tag{27}$$

$$1/r(i) = \alpha \cdot \mu(i,1) \cdot N(i,1) \cdot [Y(i) + Y(i-1)]. \tag{28}$$

(α is given from $\Sigma\, 1/r(i) = 1/R_g$; N: Impurity Concentration)

In deriving (26), the symmetry condition is assumed along the surface for simplicity. As important turn-off phenomena occur in the center of the device area, this approximation does not affect the results presented in the present paper. Gate current density $JG(i)$ is determined by (27), where resistance $r(i)$ represents the sliced p-base resistance outside the modeled region. Total gate resistance R_g is chosen to be 1 Ω in the present calculation. Gate source voltage V_g is raised at the rate of -8.0×10^6 V/s to simulate the effect of the stray inductance in the gate circuit.

As for the boundary condition for the heat equation, a fixed heat sink temperature of 300 K is assumed at the surfaces (metal contacts and the dotted lines in Fig. 2).

The actual values for the impurity profile are 1×10^{20} cm^{-3} and 15 μm for the n-emitter surface concentration and depth, 1.5×10^{18} cm^{-3} and 52 μm for the p-base or p-emitter diffusion surface concentration and depth and 2×10^{14} cm^{-3} and 150 μm for the n-base concentration and width, respectively. Device dimensions are 200 μm wide in the x-direction and 254 μm thick in the y-direction. The total emitter area is 200 μm $\times$ 5 mm. These parameters are chosen to closely represent one emitter island of the Toshiba 600-V 600-A GTO.

III. Calculated Results

Fig. 4 shows the calculated waveforms of anode voltage, anode current, and gate current. Initially, the device conducts 34 A (3400 A/cm^2) anode current.

The calculated storage time and the fall time are about 1.1 and 0.35 μs, respectively. Both numbers are smaller than the experimental results [4]. The reason is that the experiment was carried out under an inductive load condition. If a comparison is made as to the time required for the anode voltage to begin to rise, the both results show good agreement: calculated 1.1 μs, experimental 1.0 ~ 1.2 μs. Thus a better agreement can be obtained if the calculation is made under the same condition as the experiment.

Fig. 4 also shows the current density change at the center of the middle junction. The highest current density (17 000 A/cm^2) is reached early in the fall time period at $t = 1.26$ μs and $V_a = 23.5$ V. An interesting fact is that the highest current density does not appear at the end of the storage time because a high anode voltage is required to conduct the high current density in the reduced "on-region" (explanation is given later) in the p-base and middle junction, and this high anode voltage decreases anode current because of the pure resistive load nature.

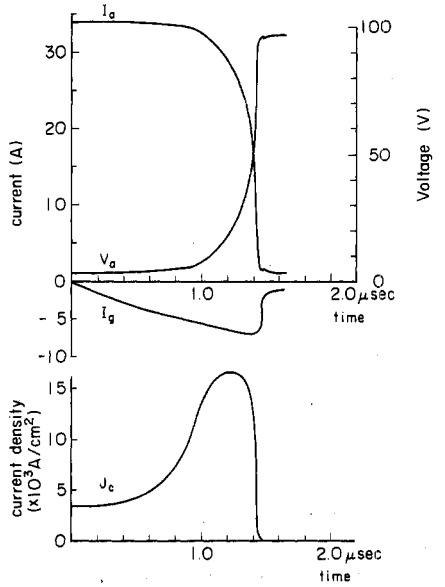

Fig. 4. Calculated turn-off waveforms and current density change at the center of the middle junction.

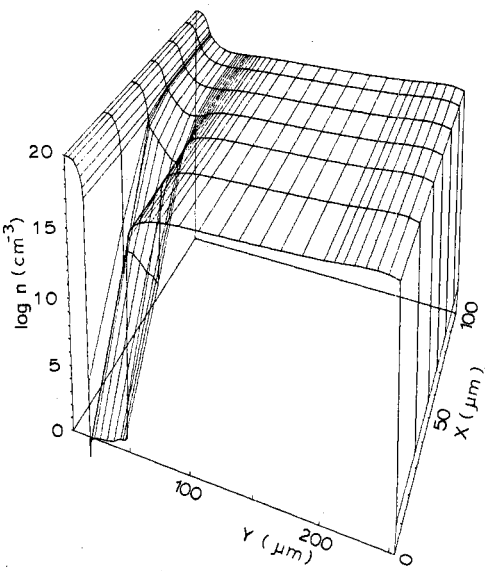

Fig. 5. Electron density distribution for $t = 0.81$ μs.

Fig. 5 shows the electron density distribution for the time of 0.81 μs. It is seen that only a part of the excess carriers (which are near the gate electrode) in the p-base and the adjacent $G \cdot K$ and middle junctions are extracted. However, all the other parts of the carrier distribution remain almost unchanged from the initial state.

From now on, "off-region" is defined especially for electrons as the area where electron density is less than 10^{14} cm^{-3}. Then, "on-region" is the rest of the device area except for the two emitter layers. The meaning of the "on-region" is that the region has a lot of injected excess carriers (excess hole density is almost the same as excess electron density). The meaning of the "off-region" is the reverse. In the "off-region," y-

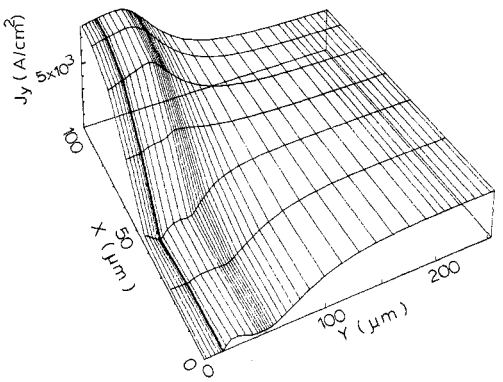

Fig. 6. Y-component of the current density distribution for $t = 0.81$ μs.

component of the current density is negligibly small, compared with the "on-region." Fig. 6 shows the y-component of the current density J_y corresponding to Fig. 5. The defined "off-region" coincides with the area where the y-component of the current density is almost zero except for the two emitters. The definitions are valid only for the two bases and the three junctions as distinguishing the two regions in emitter layers is not meaningful.

Since the on-region in the p-base in Fig. 5 is reduced to almost half of the device width, the current density in the center of the p-base is more than twice as high as the initial value. On the other hand, in the n-base, the on-region width as well as current density remain the same. Before the on-region width in the p-base reaches approximately 100 μm (before 0.9 μs), the carrier density in the on-region does not change significantly, the current density for the on-region in the p-base simply increases and anode voltage slightly increases. The present off-region includes a part of p-base, which is near the gate electrode, and the adjacent part of $G \cdot K$ and middle junctions.

As time elapses, the on-region width in the p-base reduces still further to 60 μm and stays around the same value until total anode current is turned-off, as is reported in detail in Section IV. As the on-region width in the p-base approaches this final value, 60 μm, excess carriers in the centers of the p-base and the middle junction begin to be removed, resulting in an increase in the resistance of the on-region as well as an increase in the anode voltage. Fig. 7 shows the electron density distribution for the time, 1.26 μs. The on-region width in the p-base is 64 μm, whereas the width in the n-base is still the same as the device width. The excess carriers in the middle junction of the on-region are reduced to around 10^{16} cm^{-3}. On the other hand, the excess carriers in the gate-cathode junction of the on-region are increased to more than 2×10^{18} cm^{-3} from the initial value, 1.5×10^{18} cm^{-3} because of the significant increase in current density there, which is seen in Fig. 8, where the y-component of the current density is plotted. The highest current density of 17 000 A/cm^2 is seen in the center of the middle junction. At this stage ($t = 1.26$ μs), the total anode current is still in a high value and most of the current flows in the narrow on-region in the p-base, whereas the current in the n-base still flows uniformly. If the concept "conduction region" is defined as the area within which 90 percent of the total current flows, 55 μm is obtained from Fig. 8 for the conduction region width in the p-base.

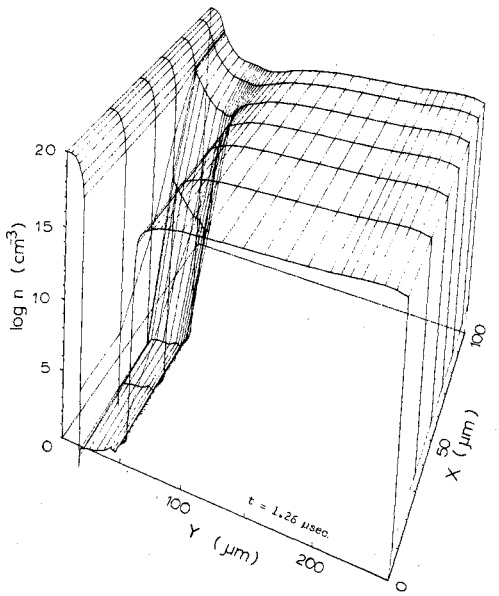

Fig. 7. Electron density distribution for $t = 1.26$ μs.

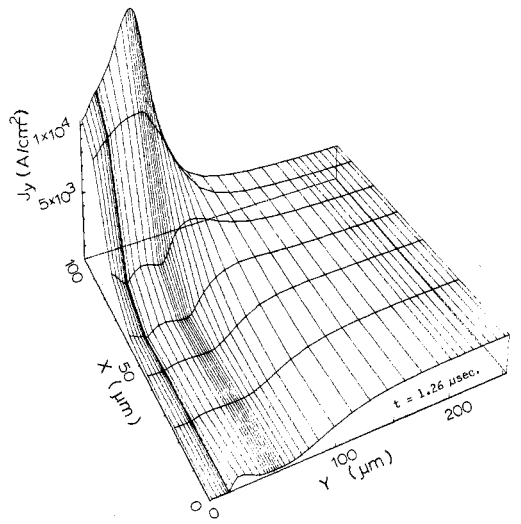

Fig. 8. Y-component of the current density distribution for $t = 1.26$ μs.

Fig. 9 shows the electric potential distribution for $t = 1.26$ μs. Only the gate-cathode junction of the on-region is still forward biased. It is seen that a large voltage drop occurs around the middle junction, even for the on-region, because current density in the on-region is significantly large and the carrier density is reduced.

After the on-region width in the p-base reaches the final value 60 μm (after 1.26 μs), the excess carriers around the middle junction of the on-region are rapidly reduced, resulting in a substantial resistance increase for the device and rapid anode voltage recovery. If the entire middle junction becomes the "off-region," the device is completely turned-off. It should be noted that a part of the device area still remains in the on-region because of the definition after the anode current is shut off. (However, the concept of "conduction region" has no meaning for this case.) Carrier density distribution in the final on-region are seen in Fig. 10, where the electron density for the device center ($X = 100$ μm) is plotted versus the y-axis.

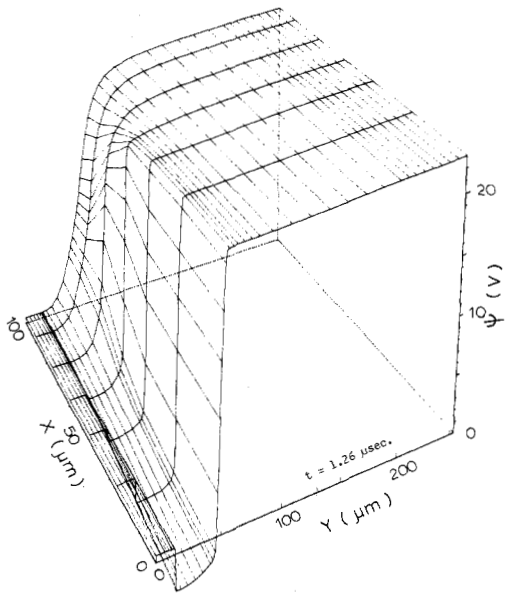

Fig. 9. Electrostatic potential for $t = 1.26$ μs.

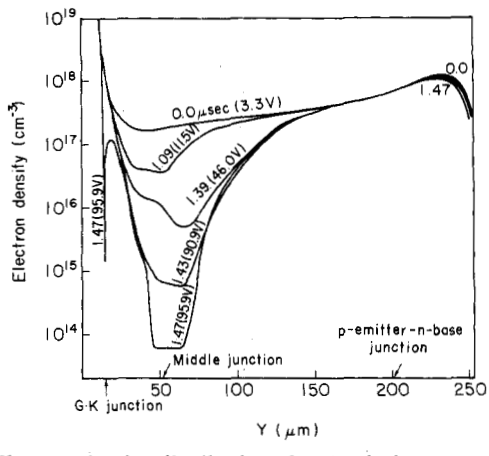

Fig. 10. Electron density distributions for the device center along $X = 100$ μm line.

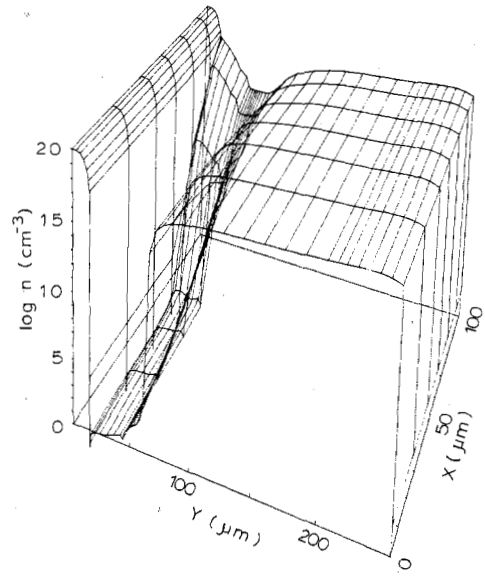

Fig. 11. Electron density distribution for $t = 1.46$ μs.

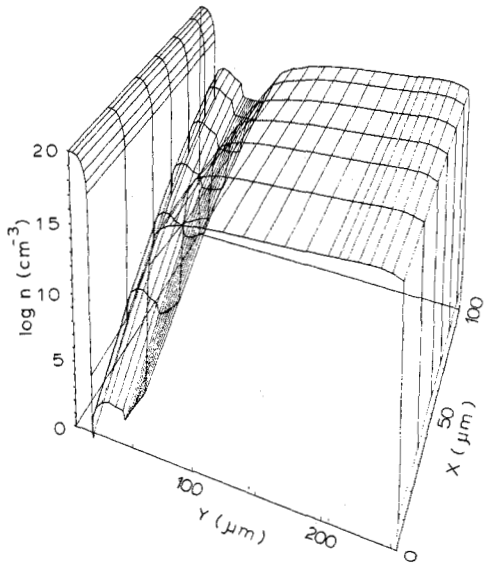

Fig. 12. Electron density distribution for $t = 1.53$ μs.

From the time of 1.09 to 1.39 μs, it is seen that a part of the excess carriers around the middle junction begin to be extracted. In the 1-D model calculation [12], it was seen that the high electric field region developed around the middle junction expanded into the n-base layer as the applied voltage increased above 100 V. However, the applied voltage is not high enough to cause the above stated phenomenon in the present case. After $t = 1.40$ μs, the carrier density in the middle junction is sufficiently reduced and the anode current is rapidly shut off. At $t = 1.47$ μs, the depletion layer ($n < N_D$: 2×10^{14} cm^{-3}) appears around the middle junction. Large excess carriers in the $G \cdot K$ junction of the final on-region are removed as the entire middle junction is depleted. Figs. 11 and 12 shows the 2-D electron density distributions just after the complete device turn-off for the time of 1.46 μ and 1.53 μs, respectively. The carrier density gradient along the x-axis in the p-base becomes less steep, corresponding to the decrease in the gate current.

Fig. 13 shows the lateral carrier density distribution in the p-base ($Y = 19$ μm) for the various time steps. The electron density gradient at the edge of the on-region is very steep. This is because a large lateral hole gate current must flow through the p-base from the inside of the on-region while the electron current is almost negligible at the edge of the on-region. The lateral hole and electron current density changes with position X along the $Y = 19$ μm line are shown in Fig. 14.

Fig. 15 shows the temperature distribution for the time of 1.47 μs. A 20-degree temperature increase is observed in the center of the middle junction. The whole distribution well reflects the current density distribution (Fig. 8) as the heat dissipation occurs almost adiabatically within 1 μs.

Fig. 16 shows the change of the on-region edge. Actually, the line represents the trace of the 10^{14} cm^{-3} electron density location on the $Y = 19$ μm line. It is found that the squeezing speed of the on-region is approximately 90 μm/μs for the pres-

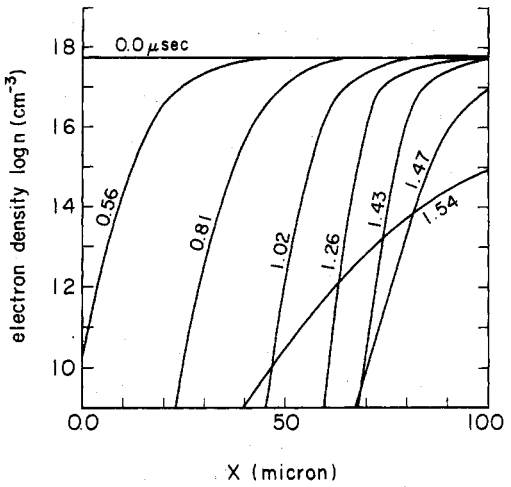

Fig. 13. Electron density distributions for various time steps along Y = 19 μm line.

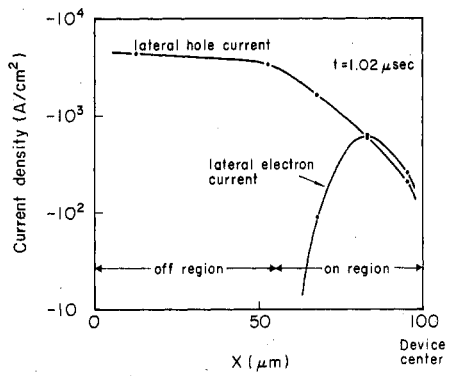

Fig. 14. Lateral current density distribution along Y = 19 μm line.

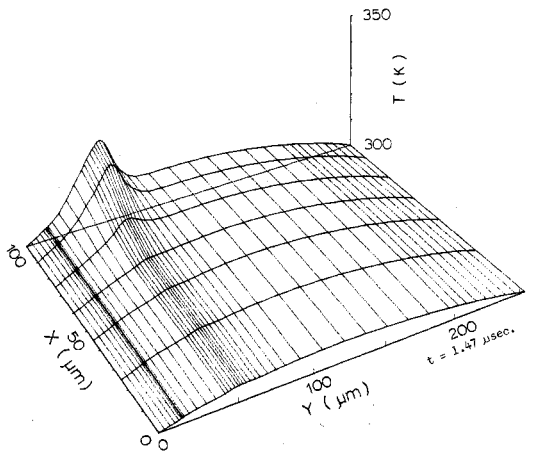

Fig. 15. Temperature distribution for t = 1.47 μs.

ent calculation. When the on-region width approaches 60 μm, the squeezing speed suddenly reduces, and the on-region width stays around 60 μm for a while. This tendency is clearly seen for an inductive load case, which is now under investigation. Results will be published in the near future [27]. The squeezing of the on-region stops when its width reaches a certain value and the whole device begins to behave like a 1-D device thereafter. It was confirmed that the half width of the final on-region coincides with the lowest obtainable ambipolar diffusion length (~25 μm) in the p-base (actually at the emitter-base junction), which is greatly reduced by carrier-to-carrier

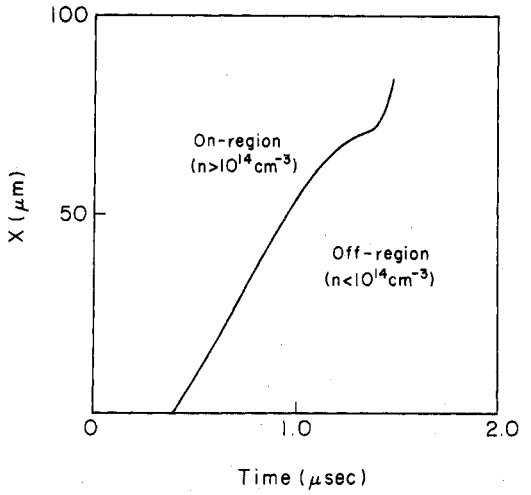

Fig. 16. Change of the conduction region edge with time.

scattering due to the high injected density of carriers (>10^{18} cm^{-3}).

The idea of the final on-region width was first introduced by Wolly [28] and was also confirmed by experiment [4], which provided the basis for the assumption adopted in the 1-D GTO turn-off model [12].

IV. Discussion

As the on-region in the p-base is reduced, the current density in the region increases significantly, causing the high injected carrier density in the $G \cdot K$ junction of the on-region as seen in Fig. 17. However, the excess carrier density in the anode side does not increase because the current density is still quite uniform there. On the other hand, the carrier density increase was observed in both sides in experiment [4] as well as in the 1-D calculation [12]. These results indicate that there should be a current density increase in the both sides in actual devices. Thus the on-region squeezing in the p-base has to take place also in the emitter-length direction. This was confirmed by the infrared observation. The squeezing in the emitter-length direction occurs in a larger scale than that in the emitter-width direction, which the present 2-D model is dealing with. For example, the on-region length in the p-base may decrease from 5 mm to less than 1 mm, whereas its width decreases from 200 or 300 μm to 60 μm. Thus the anode side current density must increase even if the n-base excess carriers remains almost unchanged. The current density in the anode side is, however, still lower than that in the cathode side. This results explains the experimental results [12] better than the 1-D model.

The most serious problem in the present calculation is the limitation in the total number of grid points, being related to the limitation of the computer time. If an accurate calculation is sought, at least 5 times more grid points will be required in the x-direction than the present number because the electron density changes very rapidly at the edge of the conduction region. This will require about 7 h CPU time on the Cyber-175 machine for only one entire turn-off process calculation. The present grid structure is probably the allowable minimum in regard to the number of grid lines in the x-direction. The authors confirmed that the results do not change very much

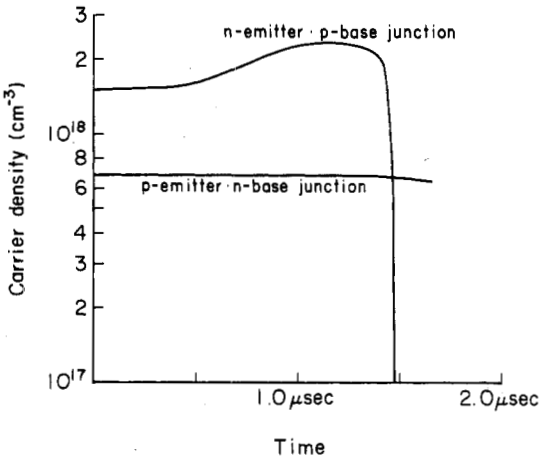

Fig. 17. Carrier density changes with time for the centers of the two emitter-base junctions.

even if the grid separation in the x-direction is reduced to almost half its value. The number of the grid lines in the y-direction is as many as 55, which may be necessary for the large applied voltage.

A second problem is that the temperature dependence is not clear for many device parameters, such as carrier lifetime and carrier mobility, especially for high densities of injected carriers and the bandgap energy for the heavily doped silicon, etc.

If it is desired to simulate device thermal degradation, more than 20 times as much heat dissipation is needed than in the present case, in addition to the above problems. One of the authors is now continuing the calculation under an inductive load condition [27], which may give more than a 100-degree temperature increase and realize a high electric field extension into the n-base, which was a phenomenon seen in the 1-D model.

V. Conclusion

Two-D model simulation of a GTO was carried out to analyze the on-region squeezing process. As the turn-off process proceeds, most parts of the excess carriers in the p-base and the adacent $G \cdot K$ and middle junctions are removed. However, n-base carriers remains almost unchanged, resulting in a uniform current distribution in the anode side in spite of the on-region squeezing in the p-base. The relatively high anode voltage (24 V in the present case) is necessary to sustain high current density (17 000 A/cm^2) in the reduced on-region. Thus the substantial anode voltage recovery is suggested for a higher anode current turn-off case when the on-region width reaches its final value. The final on-region width observed is 60 μm. One half of its width coincides with the ambipolar diffusion length in the emitter-base junction, which is the lowest value in the p-base because of carrier to carrier scattering due to the high injected carrier density. The anode current turn-off is accomplished by reducing the excess carriers around the middle junction of the final on-region.

References

[1] M. Azuma, M. Kurata, and K. Takigami, "2500-V 600-A gate turn-off thyristor (GTO)," *IEEE Trans. Electron Devices*, vol. ED-28, pp. 270–274, 1981.

[2] T. Nagano, T. Yatsuo, and M. Okamura, "Characteristics of a 3000 V, 1000 A gate turn-off thyristors," in *IEEE Conf. Rec.*, (1981 Ann. Meet. IAS), pp. 750–753, 1981.

[3] M. Azuma, A. Nakagawa, and K. Takigami, "High power gate turn-off thyristors," in *Proc. 9th Conf. on Solid State Devices*, (Tokyo, Japan), 1977; also *Japan. J. Appl. Phys.*, vol. 17 (Supplement 17-1), pp. 275–281, 1978.

[4] H. Ohashi and A. Nakagawa, "A study on GTO turn-off failure mechanism," in *IEDM Tech. Dig.*, pp. 414–417, 1981.

[5] T. Suzuki, T. Ugazin, M. Kekura, T. Watanabe, and T. Sueoka, "Switching characteristics of high power buried gate turn-off thyristor," in *IEDM Tech. Dig.*, pp. 492–495, 1982.

[6] T. Nagano, H. Fukui, T. Yatsuo, and M. Okamura, "A snubberless GTO," in *1982 PESC Rec.*, pp. 383–387, 1982.

[7] W. Anheier, W. L. Engl, O. Manck, and A. Wieder, in *IEDM Tech. Dig.*, pp. 363–366, 1975.

[8] M. Kurata, "One-dimensional calculation of thyristor forward voltage and holding current," *Solid-State Electron.*, vol. 19, pp. 527–535, 1976.

[9] M. S. Adler, "Accurate calculation of the forward drop and power dissipation in thyristors," *IEEE Trans. Electron Devices*, vol. ED-25, pp. 16–22, 1978.

[10] M. Naito, T. Nagano, H. Fukui, and Y. Terasawa, "One-dimensional analysis of turn-off phenomena for a GTO turn-off thyristor," *IEEE Trans. Electron Devices*, vol. ED-26, pp. 226–231, 1979.

[11] A. Nakagawa, "Numerical analysis on abnormal thyristor forward voltage increase due to heavy doping in gated p-base layer," *Solid-State Electron.*, vol. 24, pp. 455–459, 1981.

[12] A. Nakagawa and H. Ohashi, "A study on GTO turn-off failure mechanism—A time- and temperature-dependent 1-D model analysis," *IEEE Trans. Electron Devices*, vol. ED-31, no. 3, pp. 273–279, Mar. 1984.

[13] Y. Shimizu, M. Naito, M. Odamura, and Y. Terasawa, "Numerical analysis of turn-off characteristics for a gate turn-off thyristor with a shorted anode emitter," *IEEE Trans. Electron Devices*, vol. ED-28, pp. 1043–1047, 1981.

[14] V. C. Alwin, D. H. Navon, and L. J. Turgeon, "Time-dependent carrier flow in a transistor structure under nonisothermal conditions," *IEEE Trans. Electron Devices*, vol. ED-24, pp. 1297–1304, 1977.

[15] L. J. Turgeon and D. H. Navon, "Two-dimensional nonisothermal carrier flow in a transistor structure under reactive circuit conditions," *IEEE Trans. Electron Devices*, vol. ED-25, pp. 837–843, 1978.

[16] H. J. DeMan, "The influence of heavy doping on the emitter efficiency of a bipolar transistor," *IEEE Trans. Electron Devices*, vol. ED-18, pp. 833–835, 1971.

[17] R. J. Van Overstraeten, H. J. Deman, and R. P. Mertens, "Transport equations in heavy doped silicon," *IEEE Trans. Electron Devices*, vol. ED-20, pp. 290–298, 1973.

[18] M. S. Mock, "Transport equations in heavily doped silicon and the current gain of a bipolar transistor," *Solid-State Electron.*, vol. 16, pp. 1251–1259, 1973.

[19] H. P. D. Lanyon and R. A. Tuft, "Bandgap narrowing in moderately to heavily doped silicon," *IEEE Trans. Electron Devices*, vol. ED-26, pp. 1014–1018, 1979.

[20] J. W. Slotboom and H. C. de Graaff, "Measurements of bandgap narrowing in Si bipolar transistors," *Solid-State Electron.*, vol. 19, pp. 857–862, 1976.

[21] A. Nakagawa, "One-dimensional device model of the npn bipolar transistor including heavy doping effects under Fermi statistics," *Solid-State Electron.*, vol. 22, pp. 943–949, 1979.

[22] M. S. Adler, "An operational method to model carrier degeneracy and band gap narrowing," *Solid-State Electron.*, vol. 26, pp. 387–396, 1983.

[23] R. Stratton, "Semiconductor current-flow equations (diffusion and degeneracy)," *IEEE Trans. Electron Devices*, vol. ED-19, pp. 1288–1292, 1972.

[24] G. G. MacFarlane, T. P. McLean, J. E. Quarrington, and V. Roberts, "Fine structure in the absorption-edge spectrum of Si," *Phys. Rev.*, vol. 111, pp. 1245–1254, 1958.

[25] W. W. Gartner, *Transistors, Principles, Design, and Applications.* Princeton, NJ: Van Nostrand, 1960.

[26] R. S. Varga, *Matrix Iterative Analysis.* Englewood Cliffs, NJ: Prentice-Hall, 1962.

[27] A. Nakagawa, *Solid-State Electron.*, to be published.

[28] E. D. Wolly, "Gate turn-off in p-n-p-n devices," *IEEE Trans. Electron Devices*, vol. ED-13, pp. 590–597, 1966.